ARTICLES

Measurement of particle production in proton-induced reactions at 14.6 GeV/c

T. Abbott,[δ,(a)] Y. Akiba,[η] D. Beavis,[β] M. A. Bloomer,[ι,(b)] P. D. Bond,[β] C. Chasman,[β] Z. Chen,[β] Y. Y. Chu,[β] B. A. Cole,[ι] J. B. Costales,[ι,(c)] H. J. Crawford,[γ] J. B. Cumming,[β] R. Debbe,[β] J. Engelage,[γ] S. Y. Fung,[δ] S. Gushue,[β] H. Hamagaki,[η] O. Hansen,[β] R. S. Hayano,[κ] S. Hayashi,[η,(d)] S. Homma,[η] H. Z. Huang,[ι,(b)] Y. Ikeda,[θ,(e)] I. Juricic,[ε,(f)] J. Kang,[δ] S. Katcoff,[β] S. Kaufman,[α] K. Kimura,[θ] K. Kitamura,[ζ,(g)] K. Kurita,[ε] R. J. Ledoux,[ι] M. J. Levine,[β] Y. Miake,[β] R. J. Morse,[ι] B. Moskowitz,[β] S. Nagamiya,[ε] J. Olness,[β] C. G. Parsons,[ι] L. P. Remsberg,[β] H. Sakurai,[κ] M. Sarabura,[ι,(h)] P. Stankus,[ε] S. G. Steadman,[ι] G. S. F. Stephans,[ι] T. Sugitate,[ζ] M. J. Tannenbaum,[β] J. H. van Dijk,[β] F. Videbaek,[α,(d)] M. Vient,[δ,(i)] P. Vincent,[β,(j)] V. Vutsadakis,[ι] H. E. Wegner,[β] D. S. Woodruff,[ι] Y. D. Wu,[ε] and W. Zajc[ε]

(E-802 Collaboration)

[α]*Argonne National Laboratory, Argonne, Illinois 60439-4843*
[β]*Brookhaven National Laboratory, Upton, New York 11973*
[γ]*University of California, Space Sciences Laboratory, Berkeley, California 94720*
[δ]*University of California, Riverside, California 92521*
[ε]*Columbia University, New York, New York 10027 and Nevis Laboratories, Irvington, New York 10533*
[ζ]*Hiroshima University, Hiroshima 730, Japan*
[η]*Institute for Nuclear Study, University of Tokyo, Tanashi, Tokyo 188, Japan*
[θ]*Kyushu University, Fukuoka 812, Japan*
[ι]*Massachusetts Institute of Technology, Cambridge, Massachusetts 02139*
[κ]*Department of Physics, University of Tokyo, Tokyo 113, Japan*
(Received 27 December 1991)

Particle production in proton-induced reactions at 14.6 GeV/c on Be, Al, Cu, and Au targets has been systematically studied using the E-802 spectrometer at the BNL-Alternating Gradient Synchrotron. Particles are measured in the angular range from 5° to 58° and identified up to momenta of 5, 3.5, and 8 GeV/c for pions, kaons, and protons, respectively. Mechanisms for particle production are discussed in comparison with heavy-ion-induced reactions at the same incident energy per nucleon.

PACS number(s): 13.85.Ni, 25.40.Ve, 25.75.+r

I. INTRODUCTION

Experiments performed at the BNL Tandem–Alternating Gradient Synchrotron (AGS) Complex using heavy-ion beams of ^{16}O and ^{28}Si at 14.6 A GeV/c have produced insight into the properties of nuclear matter at high baryon density and temperature [1–3]. To clarify the reaction mechanism of these collisions, it is necessary to understand the systematics of the underlying processes such as $p+A$ reactions with a variety of targets at the same incident energy per nucleon. Unfortunately, such data at central rapidities do not exist. A systematic set of measurements of proton-induced reactions on Be, Al, Cu, and Au targets at 14.6 GeV/c has therefore been performed by the E-802 Collaboration using the same detectors as for the ^{16}O and ^{28}Si beams.

While the global variables such as the transverse neutral energy produced in the heavy-ion collisions are consistent with an incoherent superposition of contributions from individual $p+A$ reactions [1], the relative yields of the produced particles show dramatic differences from this picture. In particular, an enhanced K^+/π^+ ratio ($\approx$20%) has been observed by the E-802 Collaboration [2] in central Si+Au interactions in the central rapidity region compared with p-p interactions ($\approx$5%) at about the same incident energy per nucleon [4]. This result is

[a]Now at Xon Tech, Inc., Van Nuys, CA 91406.
[b]Now at Lawrence Berkeley Laboratory, Berkeley, CA 94720.
[c]Now at Lawrence Livermore National Laboratory, Livermore, CA 94550.
[d]Now at Brookhaven National Laboratory, Upton, NY 11973.
[e]Now at Hitachi Limited, Hitachi, Ibaraki 316, Japan.
[f]Now at Schlumberger Corporation, Houston, TX 77210.
[g]Now at NTT Tsuyama, Tsuyama, Okayama 708, Japan.
[h]Now at Los Alamos National Laboratory, Los Alamos, NM 87454.
[i]Now at University of California at Irvine, Irvine, CA 92717.
[j]Now at Bruker Medical Imaging, Inc., Lisle, IL 60532.

 ©1992 The American Physical Society

of particular interest since an enhanced strangeness production is predicted [5] as a signal for the onset of a quark-gluon-plasma (QGP) phase in heavy-ion reactions [6,7]. The observed enhancement has, however, also been discussed in thermal models [8,9] and rescattering models [10,11]. In the present measurement on $p+A$ reactions, it is observed that, as the target mass increases, the integrated yield of pions changes little while the yield for K^+ is enhanced, resulting in a gradual increase of the K^+/π^+ ratio. Furthermore, the rapidity distribution of the K^+/p ratio is nearly independent of the target mass, suggesting a relationship between the yields of protons and K^+ mesons. These results provide new information on strangeness production in heavy-ion reactions.

In this paper, the E-802 experimental setup will be briefly described. A section is devoted to a detailed description of the off-line analysis for obtaining the particle production cross sections. The systematics of particle production for proton-induced reactions are then presented together with a comparison with the results from heavy-ion-induced reactions.

II. THE E-802 MAGNETIC SPECTROMETER

The main part of the E-802 spectrometer [12] (Fig. 1) consists of a dipole magnet ($\int B\,dl \leq 1.5$ Tm) with four sets of tracking chambers (two before the magnet and two after), a 160-element time-of-flight (TOF) wall, and a 40-segment high-pressure (4-atm) gas Čerenkov counter (GASC) followed by a position-sensitive back counter (BACK). The spectrometer has a geometrical solid angle of 25 msr, and it can be rotated to cover laboratory angles from 5° to 58° in five angular settings, namely, by placing the beam side edge of the magnet at 5°, 14°, 24°, 34°, and 44°. The polar angle bite is 14°. Data are taken at each angle with both magnet polarities.

The drift chambers used for tracking are placed at distances from the target of approximately 1 ($T1$), 1.5 ($T2$), 4 ($T3$), and 4.5 m ($T4$). Each set is composed of four or five modules with wires at different angles. Local vectors of particle trajectories can be constructed in $T2$, $T3$, and $T4$ (which have a large enough separation between their planes), and only space points can be constructed for $T1$ (higher segmentation but smaller plane separation). Measured single-particle resolutions are close to 150 μm, while two-particle resolutions are about 2 mm. More details on the construction of the chambers can be found in Ref. [12].

The time-of-flight wall is placed 6.5 m away from the target position. It is made of pickets of plastic scintillator which are 78 cm high, 1.6 cm thick, and 1.6 cm wide, except for 10 special pickets of double width (which are needed because of geometrical considerations). Signals are read out through light guides by photomultipliers at each end. The timing resolution was measured picket by picket with a 15-GeV/c negative-pion beam, and an average σ of 75 ps is, at best, achieved after time slewing corrections [12]. This corresponds to a K-π separation at the 5σ level for momenta up to 2.2 GeV/c.

The newly implemented gas Čerenkov counter has 40 cells, arranged in four horizontal rows of 10 cells each, stacked one on top of the other. The cells, each with a surface area 23 cm×28 cm, are mechanically and optically segmented, and each cell is viewed by a 5-in. photomultiplier via an elliptical mirror (33 cm×38 cm). The counter is operated with 4 atm of freon-12, corresponding to an index of refraction $n=1.0045$, yielding about 10–15 photoelectrons for pions well above threshold. With the implementation of the gas Čerenkov counter, the K-π separation is extended to 5 GeV/c, and protons can be identified to 8 GeV/c, the latter with some kaon contamination between 3.5 and 5.6 GeV/c. Kaon

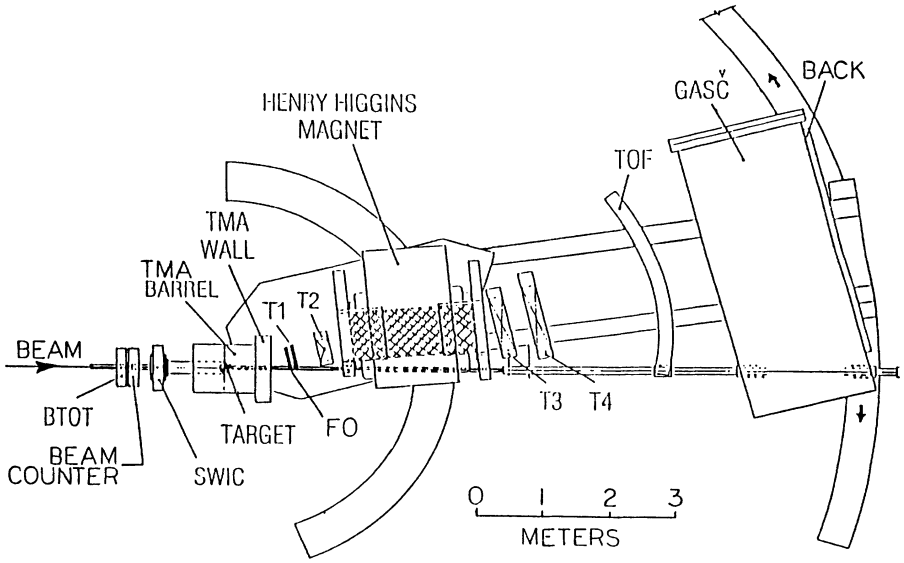

FIG. 1. A schematic layout of the E-802 spectrometer at the 5° setting. $F0$, $T1$, $T2$, the magnet, $T3$, $T4$, TOF, GASC, and BACK are described in the text. The cross-hatched area in the frame is the magnetic-field volume. The TMA barrel and TMA wall are a multiplicity counter of proportional tubes, surrounding the target. BTOT and SWIC are part of the beam counter and beam diagnostic detectors.

identification, however, is limited to 3.5 GeV/c since the TOF is unable to distinguish kaons from protons beyond this momentum.

Immediately behind the gas Čerenkov counter, there is a wall consisting of two layers of plastic streamer tubes (BACK). The tubes are operated in proportional mode and are read out by 6 cm×5 cm pads arranged in 24 rows and 64 columns. The main purpose of the wall is to confirm particles after the TOF wall and the GASC tank.

Unlike previously published E-802 heavy-ion data, this experiment is triggered on minimum-bias events by particles entering the spectrometer. This spectrometer trigger requires at least one slat of a set of 21 plastic scintillators (F0) in front of the first tracking chamber, as well as one slat in the TOF, fired in conjunction with a valid beam event.

Targets of Be (1480 mg/cm^2), Al (1630 mg/cm^2), Cu (1440 mg/cm^2), and Au (2939 mg/cm^2) were used, as well as a blank target frame for background evaluation [12].

III. ANALYSIS

The evaluation of the cross sections for particle production consists of two major tasks: the reconstruction of particle trajectories and particle identification. Since the production of strange particles is of most interest, the emphasis of this section will be on particle identification and, in particular, on K-π separation.

A. Tracking

Hit positions on the drift chambers are used to reconstruct particle trajectories. The surveyed positions of the drift chambers are adjusted slightly by examining straight tracks taken in zero magnetic field runs to produce the best alignment.

The reconstruction is started after the magnet by finding, in the horizontal direction, those $T3$ and $T4$ hit positions which form a straight line and are confirmed by a TOF wall hit within ±5 cm in the bending plane. Corresponding vertical hit positions and projections on other wire modules are searched to confirm these candidates, which are furthermore required to be confirmed by the TOF in the vertical direction within ±5 cm. The choice of a 5-cm cut on the TOF wall results from considerations of multiple scattering of the particles and the timing resolution of the TOF wall (discussed later). In order to reject background trajectories produced by secondary particles, which are copiously produced in the downstream beam pipe and on the magnet yokes, the confirmed track candidates are assumed to originate from the center of the target, and are then propagated through the magnet to the front chambers. Their projections on $T1$ and $T2$ must be confirmed by hits on the chambers within ±1 cm. Once a track is established within the search areas, a better fit to the hit positions of the chambers is performed with the position at the target location as a free parameter. A cut (2 cm) is imposed on the distance from the target center to discriminate particles produced upstream. The particle momentum p as well as the length of the trajectory, L, are calculated from the best fit.

An evaluation of the reconstruction efficiency was obtained by visual identification of tracks from the hit positions on the chambers. The results of the visual scanning were compared with results of the reconstruction program. It was concluded that, on average, 85% of all tracks were reconstructed by the program. The statistics of the visual identification was only sufficient to conclude that the variation of the reconstruction efficiency with angle and momentum is less than 10%. The final cross sections are corrected for the average reconstruction efficiency.

B. Particle identification

1. Detector calibration

The calibration of the TOF wall is performed iteratively by using the reconstructed tracks. The quantities in the calibration include the time of flight of particles, the vertical hit position on the slats, and the energy loss in the slats. The measured time of flight is the time difference between the TOF slat and the beam counter:

$$F_{\mathrm{TDS}}=T_{\mathrm{clck}}(C_{\mathrm{up}}+C_{\mathrm{dwn}})/2-T'_{\mathrm{clck}}(C'_{\mathrm{up}}+C'_{\mathrm{dwn}})/2\ , \quad (1)$$

where T_{clck} is the time-to-digital converter (TDC) conversion constant which is calibrated to be about 50 ps per channel. C_{up} and C_{dwn} stand for channel numbers for the TDC's of the up and down photomultipliers. The primed quantities correspond to those of the beam counter.

To start the calibration, negative tracks of high-momentum ($p \geq 0.8$ GeV/c) are first selected and assumed to be pions. With the pion mass assigned to the particle, an expected time of flight F_{exp}, can be calculated based on the reconstructed momentum p and flight path L in the tracking. For a given slat, the measured time of flight F_{TDC} is compared to the expected time of flight F_{exp} and the mean of the difference, denoted as F_{diff}, is determined. The time of flight of a particle in the experiment is therefore the time of flight converted from TDC's, F_{TDC}, minus the offset:

$$F_{\mathrm{mea}}=F_{\mathrm{TDC}}-F_{\mathrm{diff}}\ . \quad (2)$$

One σ resolution of 110 ps is achieved at this stage.

The timing resolution is further improved by correcting for time slewing from the use of leading edge discriminators: the pulse height from the photomultiplier varies, and jitter occurs in the timing. This variation is corrected to a large extent in software by studying the correlation of the jitter, $F_{\mathrm{mea}}-F_{\mathrm{exp}}$, and the measured energy loss in the slat, E_{loss}. Because of the exponential light attenuation in the scintillator, the energy loss in a slat is proportional to the geometrical average of the outputs from the two analog-to-digital converters (ADC's), and it is normalized by the minimum-ionizing particles. A simple method is used for the slewing correction and a typical resolution of 75–80 ps is achieved using

$$F_{\mathrm{slew}}=F_{\mathrm{mea}}-C_{\mathrm{slew}}E_{\mathrm{loss}}^{-1/2}+O_{\mathrm{slew}}\ , \quad (3)$$

where F_{mea} and F_{slew} are the measured and the slewing corrected time of flight, respectively, and C_{slew} and O_{slew} are the parameters of a linear least-squares fit of

$F_{mea}-F_{exp}$ vs $E_{loss}^{-1/2}$.

The vertical hit position on the slats, Y_{hit}, is calculated by taking the difference of the TDC's from the two photomultipliers, and it is calibrated using the projections on the TOF wall from the established trajectories. A least-squares fit over many hits on a slat is used to determine the parameters Y_{slop} and Y_{off}, defined as

$$Y_{hit}=Y_{slop}[(C_{up}-C_{dwn})-Y_{off}] . \quad (4)$$

The one σ resolution of hit positions is better than 1.2 cm.

The light yield detected by the photomultipliers of the GASC cells are first calibrated by the one photoelectron peak. A cell of the GASC detector is considered fired if its output signal is larger than 0.5 photoelectron (the typical output is 10–15 photoelectrons for high-momentum pions). The thresholds of the GASC detector with freon-12 at 4-atm pressure are 1.6 GeV/c for pions, 5.6 GeV/c for kaons, and 10.8 GeV/c for protons. Since particles may become lost because of interactions or decay in the GASC tank, the BACK counter is needed to reject these tracks from further analysis: a track is considered confirmed by the BACK counter if the projected pad or any of its neighbors are fired. Efficiencies related to these technical issues will be discussed later.

2. *Procedures and corrections*

(a) Procedures. The particle identification scheme is shown schematically in Fig. 2.

Electrons are identified up to 1.4 GeV/c by TOF and GASC ($p \leq 0.6$ GeV/c) or by GASC alone. Above 1.4 GeV/c, electrons are counted as pions, since both give light in the GASC counter and cannot be distinguished by TOF. At the low momenta and the 5° spectrometer setting, the electron yield is about 5% of the pion yield, but above 1.4 GeV/c it is smaller.

Pions below 1.4 GeV/c are identified by TOF with the condition of no light in GASC. After most of the pions have been positively identified by GASC in the momentum range $1.6 \leq p \leq 2.5$ GeV/c, the K-π separation is further improved by the TOF. Above 2.5 GeV/c, K-π separation is entirely based on GASC but confirmation from the BACK counter is demanded. Identification for pions is limited to 5 GeV/c, with the only contamination in the pion spectra from electrons above 1.4 GeV/c.

Kaons are identified uniquely by TOF up to 1.6 GeV/c. Above this, GASC distinguished $\pi+e$ from $p+K$ and TOF provides the K-p separation up to momentum of 3.5 GeV/c.

Finally, protons are identified by TOF up to 3.5 GeV/c. Above 5.6 GeV/c, kaons give light in the GASC and protons can be identified uniquely from the lighter particles by no light in GASC with confirmation from the BACK counter. The limit of proton identification is at 8 GeV/c. In the range from 3.5 to 5.6 GeV/c kaons are counted as protons, presumably a negligible contamination.

Figure 3 illustrates the quality of the K-π separation in the range $2.0 \leq p \leq 3.5$ GeV/c. The abscissa is the square of particle mass derived from the time of flight, the path length, and the momentum. The ordinate is the number of counts. The lower panel shows the distribution without any GASC information, while for the upper panel any particle which gives light in the GASC is re-

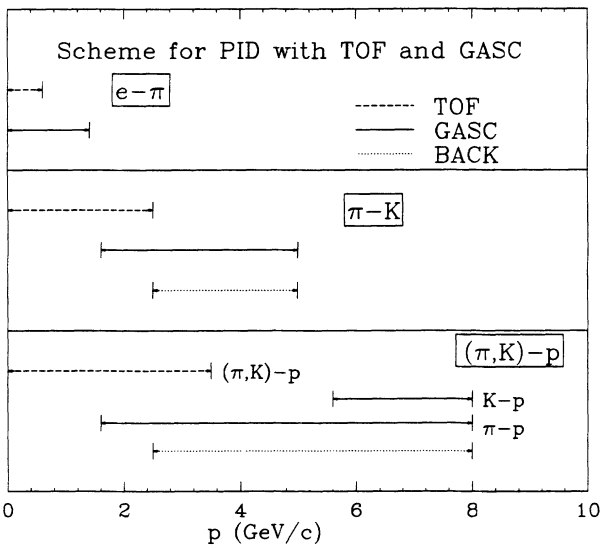

FIG. 2. The particle-identification scheme. The dash, solid, and dotted lines represent the momentum ranges in which the information from the TOF, GASC, and BACK, respectively, is used for the separation of particle pairs indicated in the figure. The different ranges of momentum for the separation of pions and kaons from protons by GASC are indicated separately.

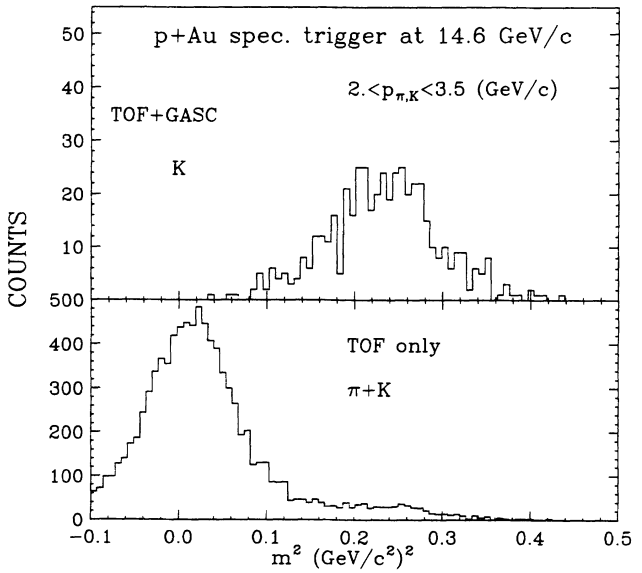

FIG. 3. The distributions of mass square for identified pions and kaons in the momentum interval $2.0 \leq p \leq 3.5$ GeV/c. The lower panel shows the distribution for pions and kaons identified by the TOF. Further rejection of pions is performed by the Čerenkov counter and the remaining kaon distribution is plotted in the upper panel. The negative value of mass square for some of the pions is because of the finite resolution (75–80 ps) of the time-of-flight measurement.

jected. Negative values on the abscissa are an artifact because of finite TOF resolution.

(b) Efficiencies and corrections. At the edges of cells in the GASC counter, the amount of light produced by high-momentum pions is found to be lower than at the center because the particle may exit the magnet with large angles with respect to the normal direction of the cell surface. However, by summing up light yields of the neighboring cells for hits on the edges, this variation is almost eliminated. When confirmed by the BACK counter, 99.5% of pions are identified by the GASC detector for momenta higher than the threshold.

The response of BACK to pions and protons can be thoroughly studied by selecting these particles with the TOF. However, the selection of kaons by the TOF is limited in momentum. Figure 4 shows the ratios of the number of tracks confirmed by the BACK to the total number of identified tracks as a function of momentum for pions, kaons, and protons. The ratios for pions and protons are very similar, and they become flat at high momentum. An assumption is made that, without decay, kaons would have the same BACK counter efficiency as pions. In other words, the efficiency for kaons is that of pions multiplied by the kaon decay probability. Since a BACK counter confirmation is assigned if the projected pad or any of its neighbors fire, the decay correction to the BACK counter has been calculated by Monte Carlo methods. The open points in Fig. 4 show the results of this assumption, and they agree well with the points measured at low momentum. Hence, this extrapolation of kaons to high momentum is adopted.

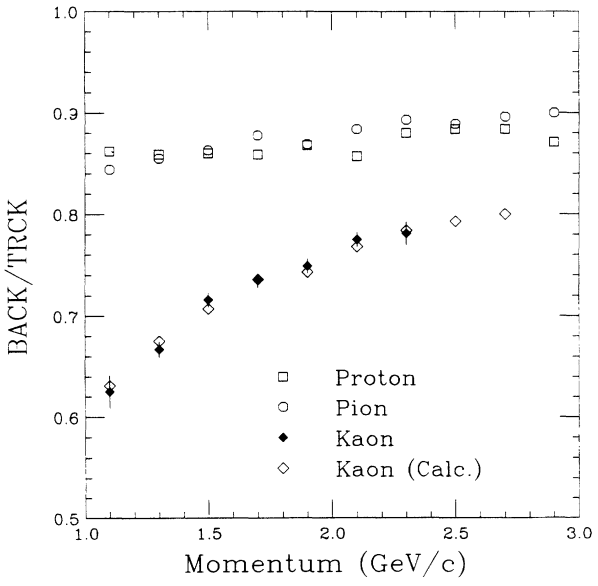

FIG. 4. The response of the BACK counter to various particles is plotted for different momenta. Open square, circle, and solid diamond are evaluated by counting the fraction of good tracks which fire the pads of BACK counter in the designated areas for protons, pions, and kaons, respectively. The open diamonds are the products of pion efficiencies and kaon decay probabilities. They coincide with data for kaons in the momentum range of TOF identification.

While the decay probability of particles from the TOF wall to the BACK counter is included in the efficiency of the BACK confirmation, the decay of kaons from the target to the TOF wall is also corrected by the survival probability as a function of momentum. For pions, however, the decay product (muons) will travel along almost the same trajectory as that of the pion so that some of these tracks are reconstructed. The pion decay correction has been studied by Monte Carlo simulations [13], and the result is used in the analysis. Because of multiple scattering, low-momentum protons are corrected for the loss introduced by various cuts (for example, target position). Gaussian fits have been performed for the distribution inside the cuts to extrapolate the fraction outside the cuts [14]. The corrections are approximately 10% at 0.5 GeV/c and become less important at higher momenta.

C. Systematic errors in normalization

After corrections for acceptance and efficiencies, tracks are sorted into bins of different kinematic variables and normalized by the number of live beam particles for the spectrometer trigger. For each bin, contributions from all of the overlapping settings are summed and normalized. For example, Fig. 5 shows accepted kinematic ranges of transverse momentum and rapidity resulting from a set of spectrometer settings of $p+\mathrm{Au}$ reaction for the identified pions, kaons, and protons, respectively, with the bins indicating where final cross sections are evaluated. Typically, about $\pm(1-2)\%$ deviation of normalization is observed for runs taken at the same spec-

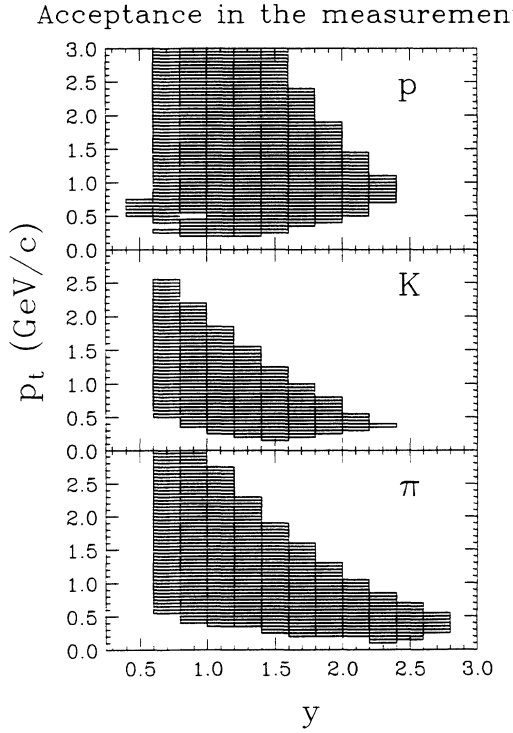

FIG. 5. An example of the acceptance coverage in transverse momentum and rapidity resulting from a typical set of spectrometer settings.

trometer settings, and ±(7–8)% for different settings within overlapping acceptance. The overall uncertainty in the normalization of the cross section is estimated to be about ±(10–15)%. The momentum spectra of pion production in $p+\mathrm{Be}$ reactions have also been compared with the measurement $p+\mathrm{Be}\rightarrow\pi^{+}+\mathrm{X}$ from the ANL Zero Gradient Sychrotron (ZGS) at 12.5 GeV/c [15]. There is a satisfactory agreement both in the spectral shapes and in absolute cross sections.

IV. INVARIANT CROSS SECTIONS

Figures 6–9 show the particle spectra, measured with the spectrometer trigger, for reactions on Be, Al, Cu, and Au targets, respectively. The spectra are presented as invariant cross sections versus transverse kinetic energy,

$$(m_{\perp}-m_0)c^2=\sqrt{(m_0c^2)^2+(p_tc)^2}-m_0c^2 .$$

There are six panels in each figure for the identified parti-

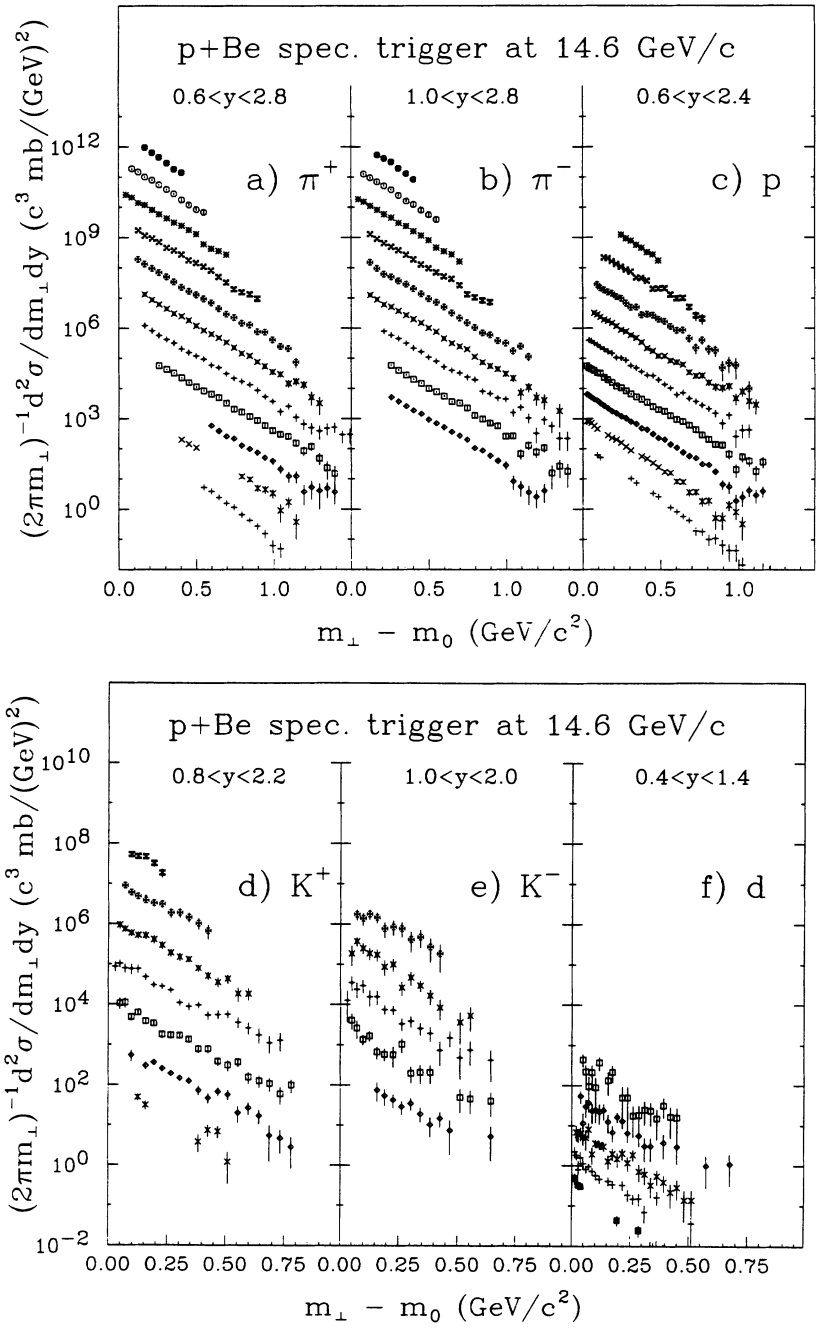

FIG. 6. Invariant cross sections as a function of $m_{\perp}-m_0$ for (a) π^{+} in $0.6<y<2.8$, (b) π^{-} in $1.0<y<2.8$, (c) protons in $0.6<y<2.4$, (d) K^{+} in $0.8<y<2.2$, (e) K^{-} in $1.0<y<2.0$, and (f) deuterons in $0.4<y<1.4$, in the proton-induced reactions on Be with a spectrometer trigger. Spectra are plotted for a rapidity interval of 0.2, and multiplied by an integral power of 10, that is, 10^{0} for $0.6<y<0.8$, 10^{1} for $0.8<y<1.0$, 10^{2} for $1.0<y<1.2$, etc. The errors show statistical uncertainties only. There is a ±(10–15)% systematic uncertainty in the absolute normalization.

cles: π^+, π^-, p, K^+, K^-, and deuterons. In each panel, spectra are binned in a rapidity interval of $\delta y = 0.2$ and are presented if more than five points, each with a minimum of 2 counts, are measured. The spectra are displaced vertically by multiplying each by powers of 10 with the bottom spectrum at the smallest rapidity. The uncertainties shown are statistical only. The low $m_\perp$ end of the spectra is cut off by the acceptance of the spectrometer, with the cutoff changing with rapidity and particle species. On the high $m_\perp$ end of the spectrum, the cutoff is determined by the particle identification (PID) limit at large rapidities and limited by statistics at low rapidities.

In general, the spectra exhibit exponential distributions. Over three or four decades there is no significant deviation from exponential shapes observed in the distributions of pions and protons. Because of poorer statistics, the spectra of kaons and deuterons have larger fluc-

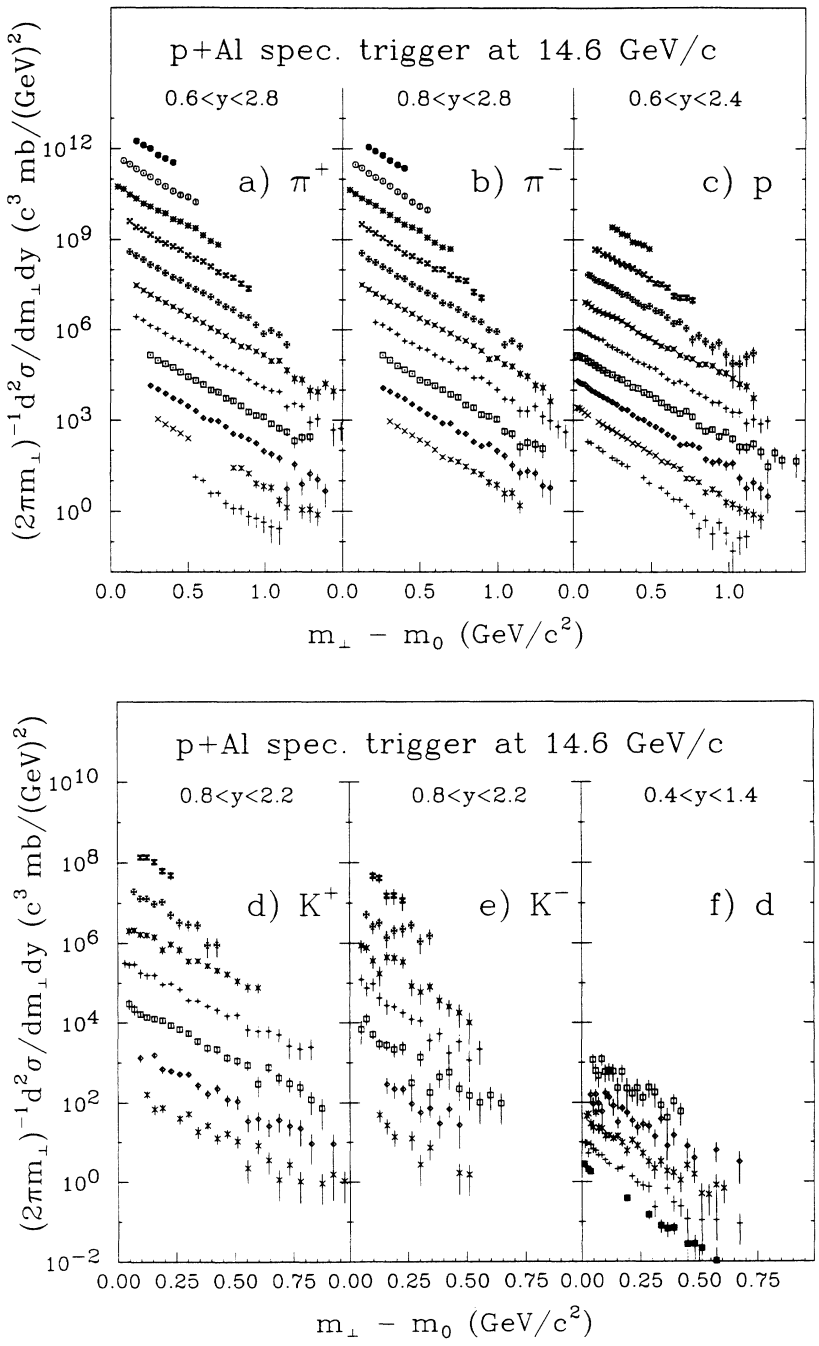

FIG. 7. Invariant cross sections as a function of $m_\perp - m_0$ for (a) π^+ in $0.6 < y < 2.8$, (b) π^- in $0.8 < y < 2.8$, (c) protons in $0.6 < y < 2.4$, (d) K^+ in $0.8 < y < 2.2$, (e) K^- in $0.8 < y < 2.2$, and (f) deuterons in $0.4 < y < 1.4$, in the proton-induced reactions on Al with a spectrometer trigger. (See caption on Fig. 6.)

tuations, but the spectra are still consistent with being exponential. The spectra, therefore, can be parametrized as

$$\frac{d^2\sigma}{2\pi m_\perp \, dm_\perp \, dy} = Ae^{-m_\perp/B} . \quad (5)$$

Figures 10–13 show systematically the fitted inverse slope parameter B, in units of MeV/c^2 for the spectra of reactions on Be, Al, Cu, and Au targets as a function of rapidity. The uncertainties indicated are statistical only, and the systematic error on B comes from the uncertainties of momentum measurement and the uncertainty of fitting over different spectrum range in $m_t - m_0$ at different rapidity (see Figs. 6–9). It is estimated that the systematic uncertainty on B is typically less than 5%. In all reactions, the B parameters for π^+ and π^- have very similar values, and the values for deuteron and proton are close to one another. For kaons, no systematic trend could be discerned because of the rather poor statistics.

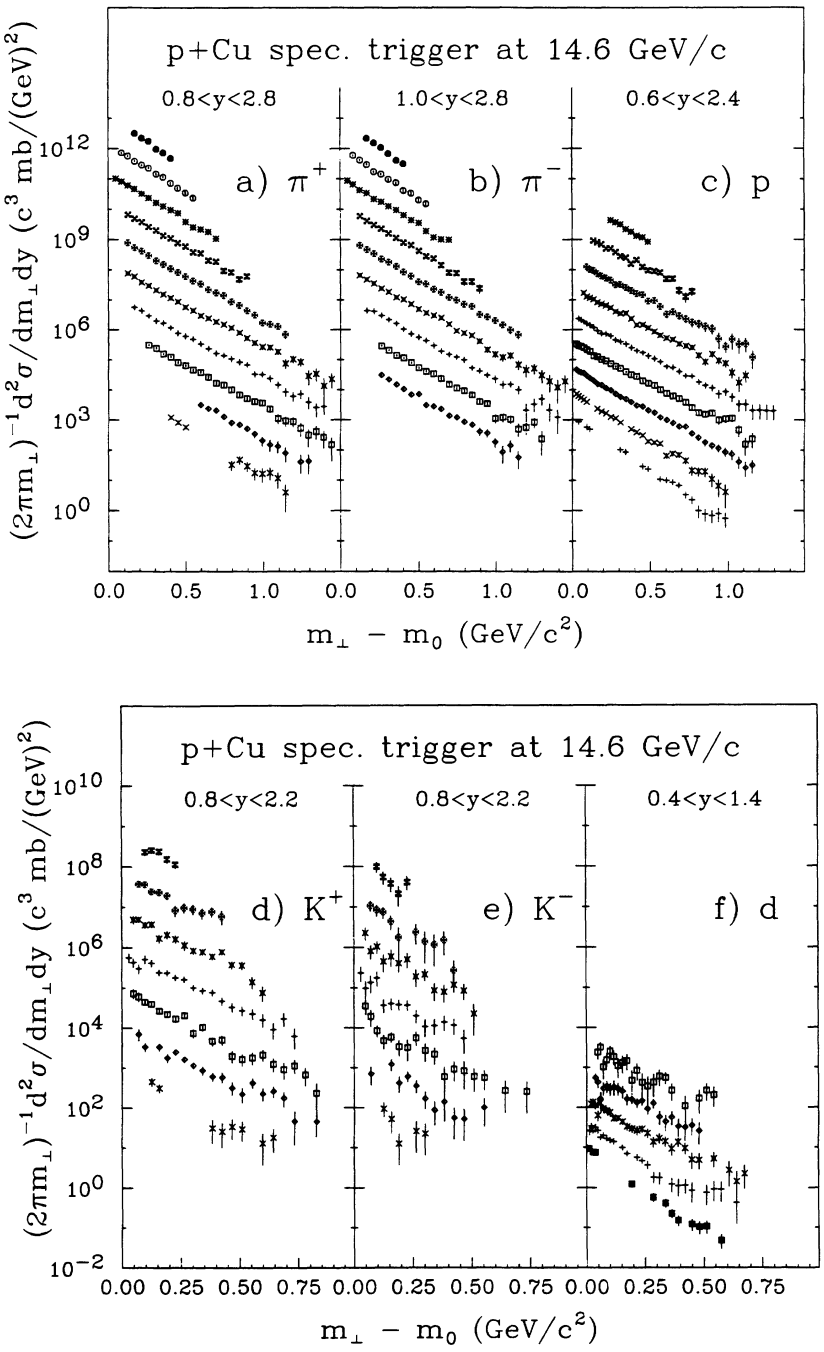

FIG. 8. Invariant cross sections as a function of $m_\perp - m_0$ for (a) π^+ in $0.8 < y < 2.8$, (b) π^- in $1.0 < y < 2.8$, (c) protons in $0.6 < y < 2.4$, (d) K^+ in $0.8 < y < 2.2$, (e) K^- in $0.8 < y < 2.2$, and (f) deuterons in $0.4 < y < 1.4$, in the proton-induced reactions on Cu with a spectrometer trigger. (See caption on Fig. 6.)

Generally, the inverse slope parameters for all the particles but kaons decrease towards both the projectile and the target rapidities.

The limited acceptance at small transverse mass introduces uncertainties in the shape of the spectra near the origin ($m_\perp - m_0 \approx 0$), and an extrapolation to this low $m_\perp$ region is needed in order to integrate the particle yields from the spectra. It is assumed in all further analysis that the spectra are exponential as described by Eq. (5) over all $m_\perp$. Therefore, the particle production yield can be integrated as follows:

$$\frac{d\sigma}{dy} = \int_{m_0}^{\infty} \int_0^{2\pi} \left[\frac{d^2\sigma}{2\pi m_\perp \, dm_\perp \, dy} \right] m_\perp \, dm_\perp \, d\phi$$

$$= 2A\pi B^2 (1 + m_0/B) e^{-m_0/B} . \quad (6)$$

Figures 14–17 show the integrated cross sections $d\sigma/dy$ as a function of rapidity for reactions on Be, Al,

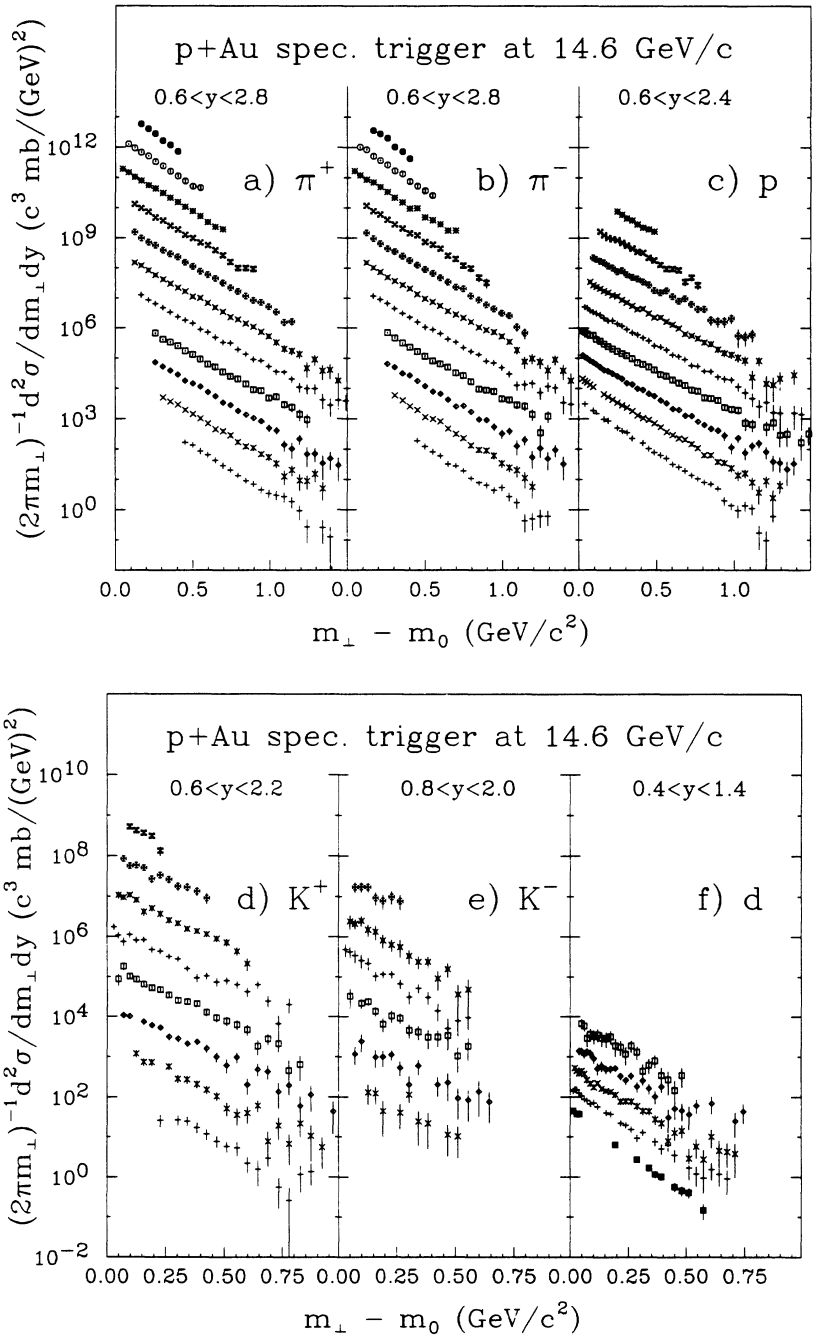

FIG. 9. Invariant cross sections as a function of $m_\perp - m_0$ for (a) π^+ in $0.6 < y < 2.8$, (b) π^- in $0.6 < y < 2.8$, (c) protons in $0.6 < y < 2.4$, (d) K^+ in $0.6 < y < 2.2$, (e) K^- in $0.8 < y < 2.0$, and (f) deuterons in $0.4 < y < 1.4$, in the proton-induced reactions on Au with a spectrometer trigger. (See caption on Fig. 6.)

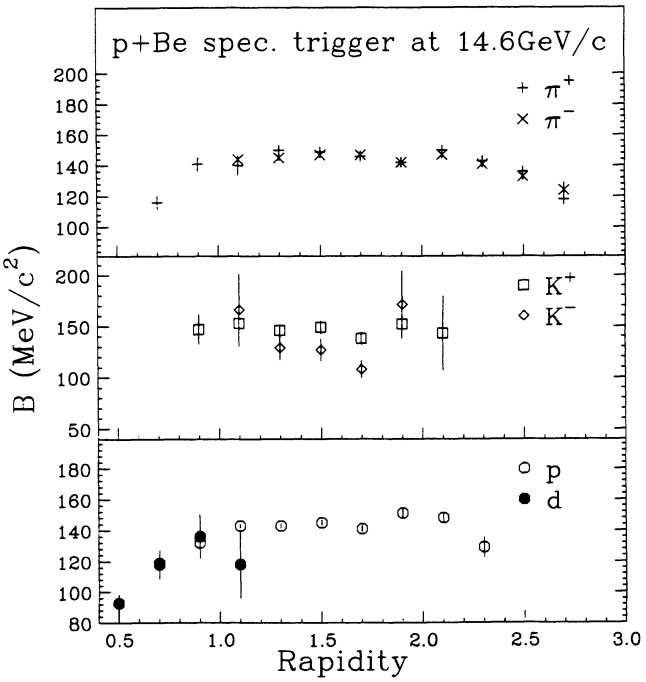

FIG. 10. Rapidity distributions of inverse slope parameters B in units of MeV/c^2 for $\pi^{\pm}$, $K^{\pm}$, protons, and deuterons in the proton-induced reactions on Be with a spectrometer trigger. The errors show statistical uncertainties only.

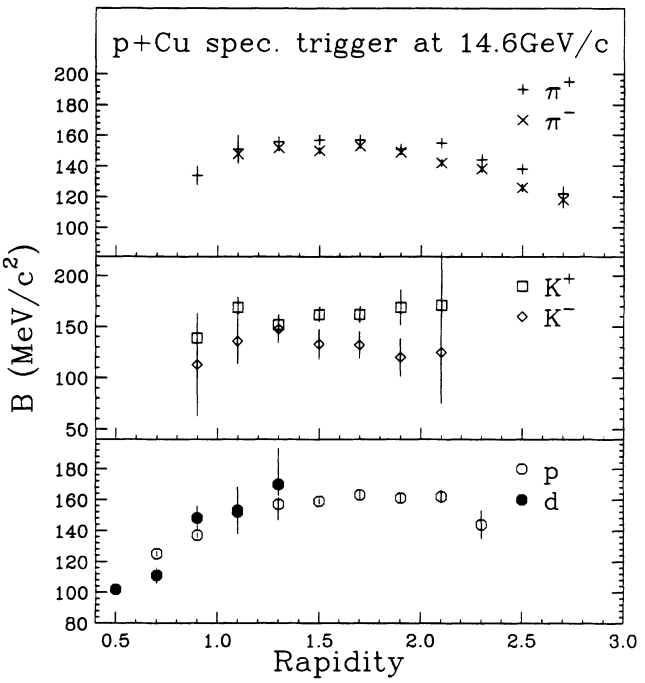

FIG. 12. Rapidity distributions of inverse slope parameters B in units of MeV/c^2 for $\pi^{\pm}$, $K^{\pm}$, protons, and deuterons in the proton-induced reactions on Cu with a spectrometer trigger.

Cu, and Au targets, respectively. Pions, kaons, protons, and deuterons are included in the figures, and the uncertainties shown are statistical only. The points are placed in the center of the rapidity interval in which the data were binned.

In order to compare the particle production in each collision for various targets, the $d\sigma/dy$ spectra of Figs. 14–17 are renormalized to each interacting projectile

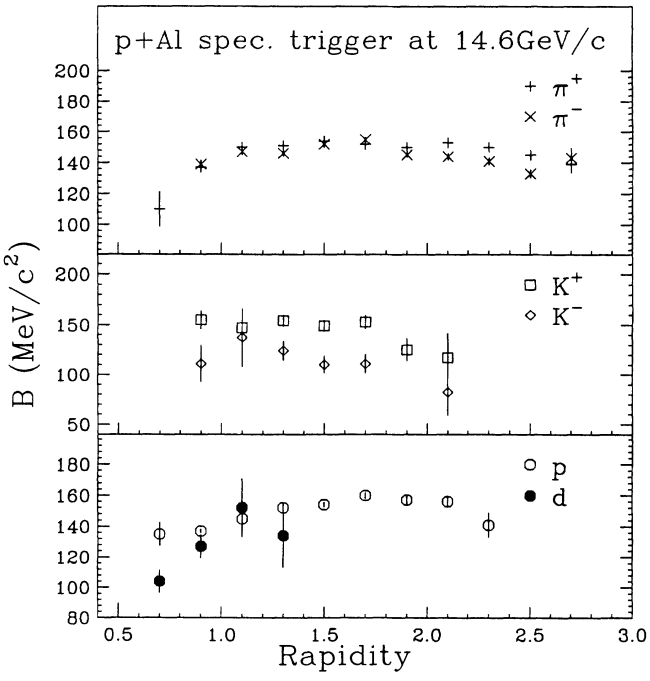

FIG. 11. Rapidity distributions of inverse slope parameters B in units of MeV/c^2 for $\pi^{\pm}$, $K^{\pm}$, protons, and deuterons in the proton-induced reactions on Al with a spectrometer trigger.

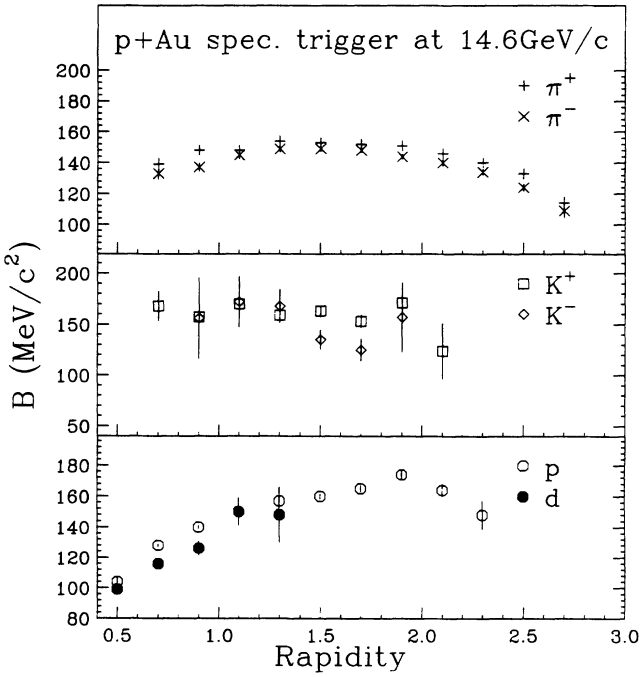

FIG. 13. Rapidity distributions of inverse slope parameters B in units of MeV/c^2 for $\pi^{\pm}$, $K^{\pm}$, protons, and deuterons in the proton-induced reactions on Au with a spectrometer trigger.

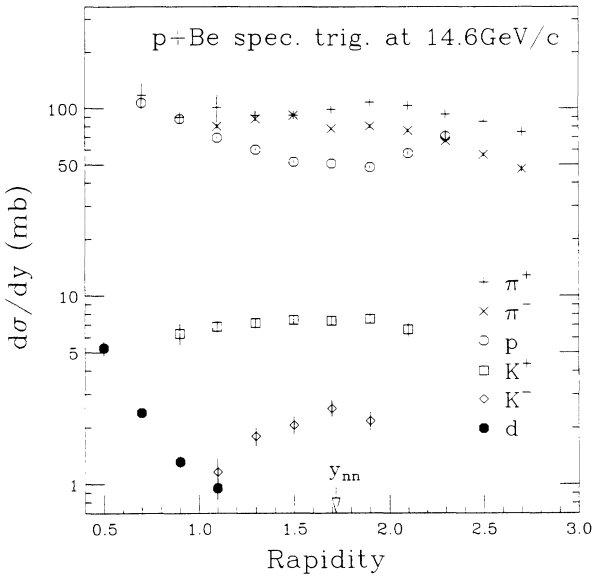

FIG. 14. Rapidity distributions of integrated cross section $d\sigma/dy$ for $\pi^{\pm}$, $K^{\pm}$, protons, and deuterons in $p+$Be collisions obtained with a spectrometer trigger. The rapidity of nucleon-nucleon center of mass, $y_{nn}=1.72$, is also shown. The errors show statistical uncertainties only.

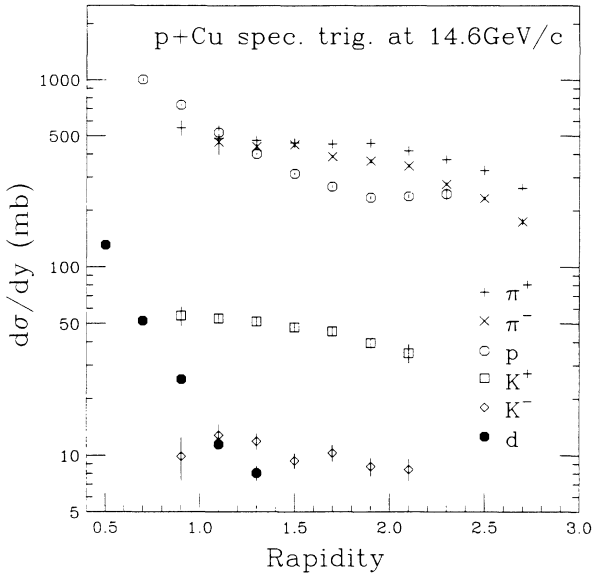

FIG. 16. Rapidity distributions of integrated cross section $d\sigma/dy$ for $\pi^{\pm}$, $K^{\pm}$, protons, and deuterons in $p+$Cu collisions obtained with a spectrometer trigger.

proton (see Fig. 19), namely,

$$\frac{dn}{dy}=\frac{1}{\sigma_{\text{inel}}}\frac{d\sigma}{dy}\ , \tag{7}$$

where σ_{inel} is the inelastic cross section for pA collisions. There are some uncertainties in σ_{inel}, especially for the proton-induced reactions on light targets. Measured inelastic cross sections [16,17] are tabulated in Table I. For comparison, the geometrical cross section of the targets is

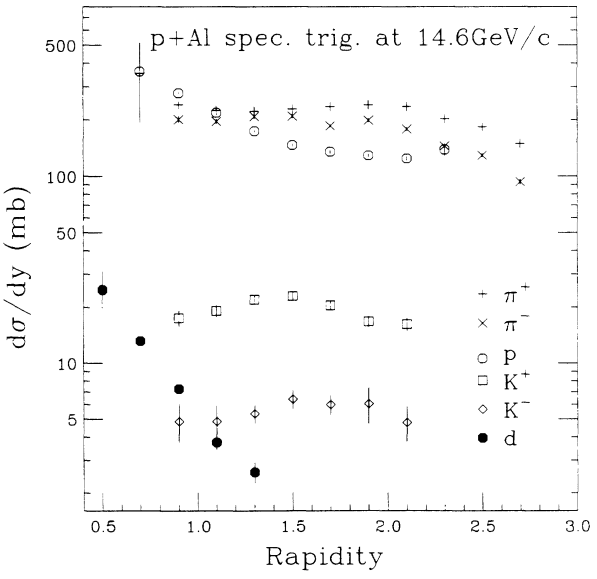

FIG. 15. Rapidity distributions of integrated cross section $d\sigma/dy$ for $\pi^{\pm}$, $K^{\pm}$, protons, and deuterons in $p+$Al collisions obtained with a spectrometer trigger.

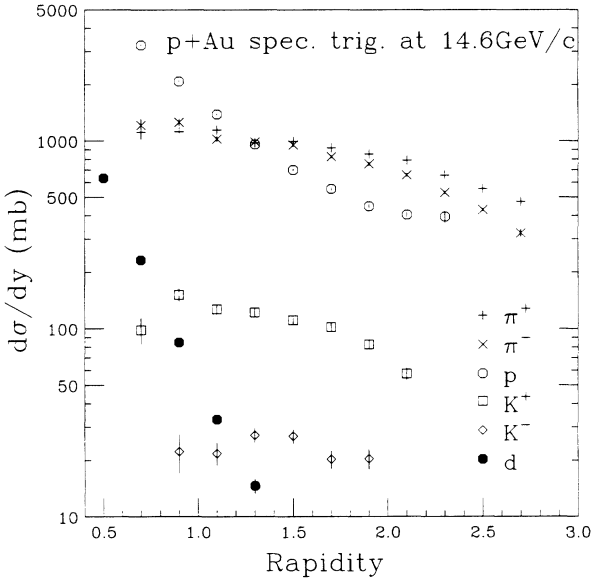

FIG. 17. Rapidity distributions of integrated cross section $d\sigma/dy$ for $\pi^{\pm}$, $K^{\pm}$, protons, and deuterons in $p+$Au collisions obtained with a spectrometer trigger.

TABLE I. Comparison of inelastic cross sections. $\sigma^{\dagger}_{\text{inel}}$ is the measured cross section from Ref. [16] at 20 GeV/c. $\sigma^{\ddagger}_{\text{inel}}$ is the measured cross section from Ref. [17] at 20 GeV/c. σ_{geo} is the geometrical cross section of the target, $\pi(1.2A^{1/3})^2$.

	$\sigma^{\dagger}_{\text{inel}}$ (mb)	$\sigma^{\ddagger}_{\text{inel}}$ (mb)	σ_{geo} (mb)
$p+$Be	208	227	196
$p+$Al	446	472	407
$p+$Cu	797	850	724
$p+$Au	1790	1750	1530

also listed as $\sigma_{geo}=\pi(1.2A^{1/3})^2$. The comparison between the measurements ($\sigma^{\dagger}_{inel}$ and $\sigma^{\ddagger}_{inel}$) indicates an uncertainty of approximately 10%. We choose the measured total inelastic cross sections of Ref. [16] at incident momentum 20 GeV/c, slightly higher than 14.6 GeV/c used in the present experiment, for the normalization.

V. COMPARISONS AND DISCUSSION

Figure 18 compares the target dependency of the inverse slope parameters B for π^+ and protons. There is little change in B for π^+ from $p+$Be (150±1.3 MeV for $1.2\le y\le 1.4$, for example) to $p+$Au (154±1.9 MeV for $1.2\le y\le 1.4$) reactions. This B value is also similar to that observed in the pion spectra from central Si+Au reactions (162±3.6 MeV for $1.2\le y\le 1.4$) [2].

The distribution of the inverse slope parameter for protons, however, changes gradually with target. For the high-rapidity protons ($y\ge 1.2$), the inverse slope parameter becomes larger for heavier targets, increasing from 150 to 175 MeV at rapidity $y=2.0$ from $p+$Be to $p+$Au with a minimum bias trigger. In heavier targets, the projectile proton suffers an increasing number of interactions due to the larger number of participant nucleons in the target, and the effect of these interactions is to increase the average transverse momentum. In central Si+Au reactions, the inverse slope parameter for protons is further increased (the highest is 240±2.7 MeV for $1.4\le y\le 1.6$), presumably since nucleons in both the projectile and the target can collide with several nucleons. In contrast, protons at low rapidities ($y\le 1$) from $p+A$ reactions are most likely target nucleons and struck only once by the single projectile proton, and their inverse slope parameters show little target dependence, with values similar to those of pions.

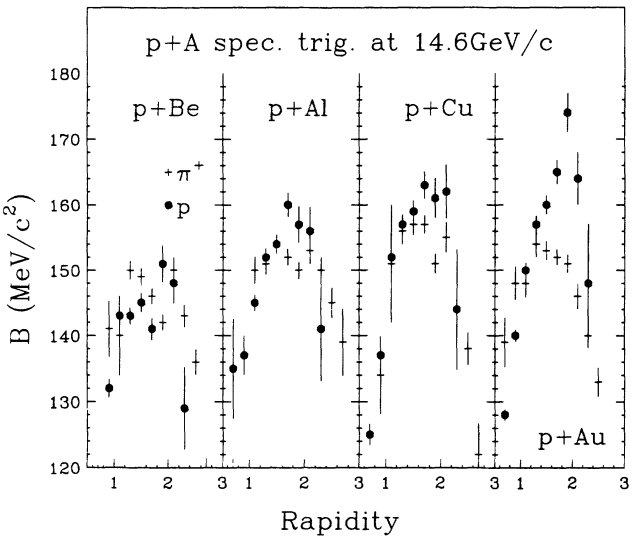

FIG. 18. A comparison of inverse slope parameters for π^+ (cross point) and protons (solid point) as a function of rapidity in $p+$Be, $p+$Al, $p+$Cu, and $p+$Au collisions obtained with a spectrometer trigger. The errors show statistical uncertainties only.

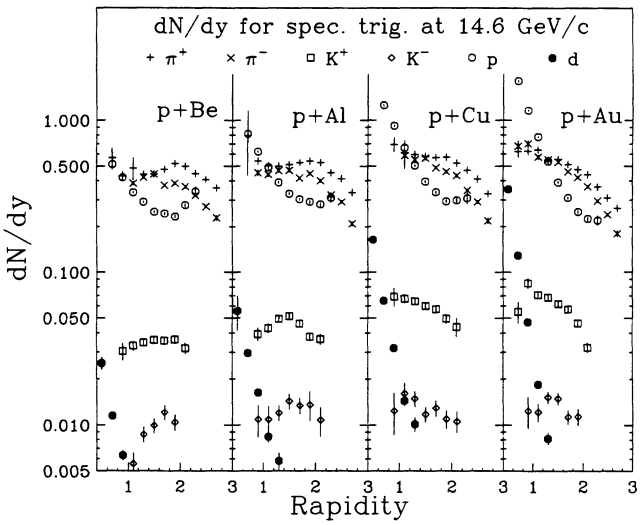

FIG. 19. Rapidity distributions of dn/dy for $\pi^{\pm}$, $K^{\pm}$, protons, and deuterons in $p+$Be, $p+$Al, $p+$Cu and $p+$Au collisions. The dn/dy is normalized to the inelastic cross sections from Ref. [16] for these reactions. The errors show statistical uncertainties only.

Figure 19 shows the normalized spectra of dn/dy [see Eq. (7)] for the reactions on Be, Al, Cu, and Au targets. The dn/dy distributions of $p+$Be (the first panel) for all particles but deuterons are very broad, and for protons it exhibits an approximate symmetry around the nucleon-nucleon center-of-mass rapidity ($y_{NN}=y_{beam}/2=1.72$), indicating that these collisions are dominated by single nucleon-nucleon collisions. Their cross section rises towards the rapidities of projectile (3.4) and target (0) and exhibit a minimum at y_{nn}. Pions and kaons are created particles, and the maxima of their cross sections are located around the central rapidity y_{nn}. The π^+ spectrum is distributed somewhat forward and its yield is about 30% more than that of π^- at high rapidities ($y\ge 2$). This is consistent with fragmentation of the proton projectile. As in p-p reactions, kaons, with a finite strangeness quantum number, have smaller yields than pions. The positive kaons show a relatively flat rapidity distribution while the negative kaons seem to be distributed narrowly around y_{nn}, reflecting their different production mechanisms: K^-'s are produced as a pair with K^+'s, while K^+'s can also be produced in association with strange baryons such as Λ. In the measured kinematic region there are roughly four times more K^+ than K^-. Deuterons are mainly located in the low-rapidity ranges, and their yields decrease quickly toward higher rapidity.

As the mass of the target increases, there are gradual changes in both the magnitude and shape of the rapidity distribution. The maxima of the produced particles $\pi^{\pm}$,$K^{\pm}$, shift towards the target rapidity. The yield of protons decreases in the forward rapidity, which is consistent with the intuitive picture that, as more target nucleons are involved in the reaction, the projectile protons may interact more times and are further shifted down in rapidity. With larger uncertainties, the K^- distribution may show the same shift. In contrast with the distribu-

tion for $p+$Be, the particle distributions for $p+$Au are not symmetric around y_{nn} but are shifted toward target rapidity. There are still more positive than negative pions in the forward rapidity, but the difference is reduced compared with $p+$Be. Relative to the other particles, deuteron yields increase most significantly with the target mass.

Figure 20 compares the relative yields, normalized to the yields in $p+$Be, of $\pi^{\pm}, K^{\pm}$, and protons for different targets as a function of rapidity. For protons, a strong enhancement towards the target rapidity is observed for the heavy target, while the ratios decrease in the forward rapidities. The ratio $(dn/dy)^{p}_{pAu}/(dn/dy)^{p}_{pBe}$ changes from 0.6 to 3.5 over the measured rapidity range. Pions have a similar but less pronounced dependence on target mass. Kaons, however, show an enhancement at all rapidities, especially at lower rapidity, where the ratio is close to that of protons.

While the shape of the dn/dy distributions changes significantly for pions from $p+$Be to $p+$Au, the integrated yield over the measured rapidity of pions does not change very much. This is not true for kaons, and one sees a steady increase of kaon yield with the target mass. Since the shapes of the distribution change and the cross sections are measured over a limited rapidity range, it is difficult to make a direct comparison of total yields of particle production for the various targets. In the measured region of kinematics, $0.6 \le y \le 2.6$ for pions, $0.6 \le y \le 2.2$ for kaons, and $0.6 \le y \le 2.4$ for protons, the ratios of the integrated yields of $p+$Au to $p+$Be are 1.08 ± 0.03 for π^+, 1.27 ± 0.05 for π^-, 1.81 ± 0.18 for K^+, and 1.95 ± 0.02 for protons. The ratios for pions are markedly smaller than that for K^+. It is curious that the increase of K^+ and protons as a function of target mass are similar and much larger than that of pions (see below).

While the pion yield remains roughly constant from $p+$Be to $p+$Au, the K^+ yield, as mentioned above, increases substantially. This causes an increased K^+/π^+ ratio for heavier targets, as indicated in Fig. 21. The top panel shows the ratio K^+/π^+, and the bottom panel the ratio K^-/π^-. For example, in the rapidity range $1.2 \le y \le 1.4$, we observe a gradual change of K^+/π^+ ratios: $(7.8\pm0.4)\%$, $(9.9\pm0.5)\%$, $(10.8\pm0.6)\%$, and $(12.5\pm0.6)\%$ for $p+$Be, $p+$Al, $p+$Cu, and $p+$Au, respectively. In the region of small rapidity, the increase of this ratio is more dramatic with increasing target mass. Still larger increases of this ratio have been observed for central Si+Au reactions [$(19.3\pm0.9)\%$ for $1.2 \le y \le 1.4$]. Better statistics are needed to conclude on any target mass dependence in the K^-/π^- ratios. The K^+/π^+ and K^-/π^- ratios obtained for $p+$Be are close to those from p-p data [4]. The result that the K^+/π^+ ratio increases with the target mass is somewhat surprising. At AGS energies and below, the K^+ yield in $p+p$ interactions decreases faster with decreasing energy than the π^+ yield [18]. In a naive picture of successive collisions of the projectile proton with target nucleons in heavy targets, a decreasing ratio is expected.

It is of interest to compare the multiplicity of created particles divided by the multiplicity of the protons for the different targets. Figure 22 displays the π^+/p and K^+/p ratios as a function of rapidity for all the targets. The π^+/p ratios, as indicated in the upper row of the figure, decreases systematically with increasing target mass at backward rapidities ($y \le y_{nn}$), and is approximately con-

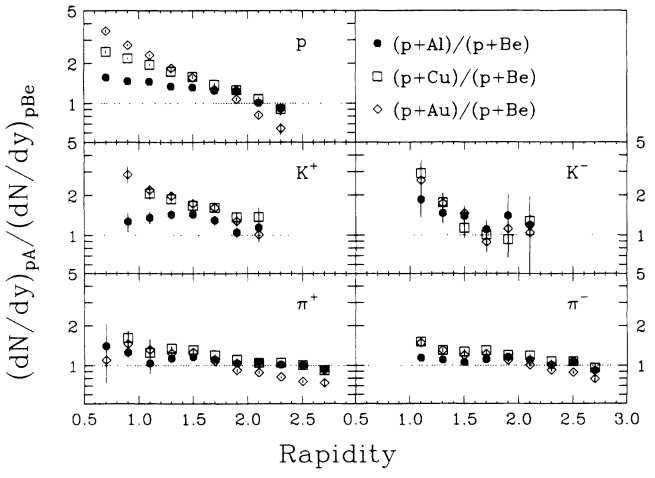

FIG. 20. Ratios of $(dn/dy)_{pA}/(dn/dy)_{pBe}$ as a function of rapidity for $\pi^{\pm}$, $K^{\pm}$, and protons. The reference lines of ratio 1 are also drawn in the figure. The errors show statistical uncertainties only.

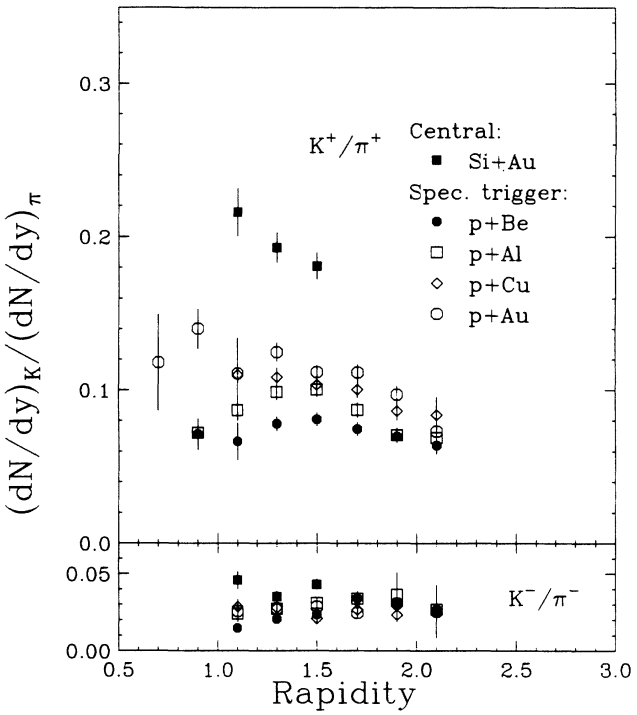

FIG. 21. K/π ratios as a function of rapidity for $p+$Be (solid circle), $p+$Al (open square), $p+$Cu (diamond), and $p+$Au (open circle) reactions for the spectrometer trigger. For comparison, also plotted are the ratios for central Si+Au (solid square) reactions [2]. The upper and lower panels show the ratios for positive and negative particles, respectively. The errors show statistical uncertainties only.

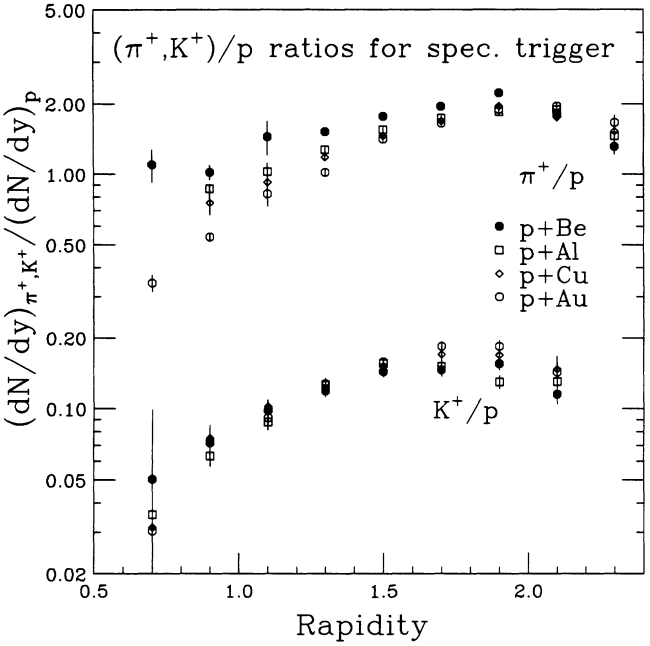

FIG. 22. Rapidity distributions of π^+/p and K^+/p ratios for $p+$Be (solid circle), $p+$Al (open square), $p+$Cu (open diamond), $p+$Au (open circle) collisions of spectrometer trigger at 14.6 GeV/c.

stant in the rapidity region forward of y_{nn}.

The rapidity dependence of K^+/p is just as strong as that for π^+/p. However, the K^+/p ratios exhibit a remarkable target mass independence. This target mass independency is in marked contrast to the ratio for pions. Stated in another way, in the backward rapidity region, for every proton observed at a given rapidity in the collision there is a definite probability of finding a K^+ at the same rapidity regardless of the target. This is a surprise and a stringent test of any proposed reaction models.

VI. SUMMARY

Measurements of particle production in proton-induced reactions at 14.6 GeV/c on Be, Al, Cu, and Au targets have been performed at the BNL AGS with the E-802 spectrometer. The yields of $\pi^{\pm}$, $K^{\pm}$, protons, and deuterons have been identified by time of flight and the segmented gas Čerenkov counters to momenta of 5, 3.5, and 8 GeV/c, respectively. Measured spectra are extrapolated in $m_\perp$ as a single exponential distribution and integrated over $m_\perp$ to obtain dn/dy. The shapes of particle distributions as a function of rapidity change from $p+$Be to $p+$Au reactions, with more particles, especially K^+, produced at lower rapidity and fewer particles towards projectile rapidity for heavy targets. While the inverse slope parameter of protons increases systematically with increasing target mass, the parameter for pions is remarkably constant from $p+$Be to $p+$Au reactions. The K^+/π^+ ratio shows a systematic increase as a function of target mass. The yield ratio of K^+/p remains constant at a given rapidity for the range of targets measured, in marked contrast to the π^+/p ratio. While a clear explanation for the enhancement of K^+ production by heavy targets is lacking, it clear that there is an evolutionary increase in the K^+ yield with the projectile and target mass.

ACKNOWLEDGMENTS

The authors would like to thank the AGS staffs for providing the proton beam. This work has been supported by the U.S. Department of Energy under contracts with ANL (W-31-109-ENG-38), BNL (DE-AC02-76CH00016), Columbia University (DE-FG02-86-ER40281), MIT (DE-AC02-76ER03069), UC Riverside (DE-FG03-86ER40271), and by NASA (NGR-05-003-513), under contract with the University of California, and by the U.S.-Japan High Energy Physics Collaboration Treaty.

[1] E802 Collaboration, T. Abbott *et al.*, Phys. Lett. B **197**, 285, (1987).
[2] E802 Collaboration, T. Abbott *et al.*, Phys. Rev. Lett. **64**, 847 (1990).
[3] E814 Collaboration, J. Barrette *et al.* Phys. Rev. Lett. **64**, 1219 (1990).
[4] J. V. Allaby *et al.*, CERN Report No. 70-12, 1970 (unpublished); H. Bøggild *et al.*, Nucl. Phys. **B57**, 77 (1973); D. Dekkers *et al.*, *ibid.* **B57**, 77 (1973); U. Becker *et al.*, Phys. Rev. Lett. **37**, 1731 (1976).
[5] J. Rafelski and R. Hagedorn, in *Thermodynamics of Quarks and Hadrons,* edited by H. Satz (North-Holland, Amsterdam, 1981), p. 253; J. Rafelski, Phys. Rep. **88**, 331 (1982).
[6] P. Koch, B. Mueller, and J. Rafelski, Phy. Rep. **142**, 167 (1986).
[7] B. Mueller, in *Hadronic Matter in Collision 1988,* Proceedings, Tucson, Arizona, 1988, edited by P. Carruthers and J. Rafelski (World Scientific, Singapore, 1989), p. 739.
[8] J. Cleymans, H. Satz, E. Suhonen, and D. W. Von Oertzen, Phys. Lett. B **242**, 111 (1990).
[9] C. M. Ko and L. Xia, Phys. Rev. C **38**, 179 (1988); C. M. Ko *et al.*, in *Quark Matter '88,* Proceedings of the Seventh International Conference on Ultrarelativistic Nucleus-Nucleus Collisions, Lenox, Massachusetts, 1988, edited by G. Baym, P. Braun-Munzinger, and S. Nagamiya [Nucl. Phys. **A498**, 561c (1989)].
[10] R. Mattiello *et al.*, Phys. Rev. Lett. 63, 1459 (1989).
[11] C. Wei-qin *et al.*, Institute of High Energy Physics Report No. BIHEP-TH-89-37 (unpublished); Institute of Theoretical Physics Report No. AS-ITP-89-20 (unpublished).
[12] E802 Collaboration, T. Abbott *et al.*, Nucl. Instrum. Methods A 290, 41 (1990).
[13] C. Parsons, Ph.D thesis, Massachusetts Institute of Technology, 1992.
[14] H. Huang, Ph.D thesis, Massachusetts Institute of Technology, 1990, pp. 65, 95.
[15] R. A. Lundby *et al.*, Phys. Rev. Lett. **14**, 504 (1965).

[16] S. P. Denisov, S. V. Donskov, Yu. P. Gorin, R. N. Krasnokutsky, A. I. Petrukhin, Yu. D. Prokoshkin, and D. A. Stoyanova, Nucl. Phys. **B61**, 62 (1973).
[17] G. Bellettini, G. Cocconi, A. N. Diddens, E. Lillethun, G. Matthiae, J. P. Scanlon, and A. M. Wetherrell, Nucl. Phys. **79**, 609 (1966).
[18] E. Albini *et al.*, Nucl. Phys. **B84**, 269 (1975).